KSME

Springer

Journal of Mechanical Science and Technology 37 (1) 2023

Original Article
DOI 10.1007/s12206-022-1219-y

Keywords:
· Axial fan
· Design optimization
· Multi-objective
· Surrogate model
· Parameterization
· Computational fluid dynamics

Correspondence to:
Tao Jin
cejintao@zju.edu.cn

Citation:
Kong, C., Wang, M., Jin, T., Liu, S. (2023). The blade shape optimization of a low-pressure axial fan using the surrogate-based multi-objective optimization method. Journal of Mechanical Science and Technology 37 (1) (2023) 179~189. http://doi.org/10.1007/s12206-022-1219-y

Received May 2nd, 2022
Revised August 10th, 2022
Accepted September 25th, 2022

† Recommended by Editor Han Seo Ko

The blade shape optimization of a low-pressure axial fan using the surrogate-based multi-objective optimization method

Chuang Kong[1], Meng Wang[1], Tao Jin[1] and Shaoliang Liu[2]

[1]College of Energy Engineering, Zhejiang University, Hangzhou 310027, China, [2]Suzhou Sigma Technology Co., LTD, Suzhou 215000, China

Abstract As a core component of a fan, the blade has a decisive impact on the aerodynamic performance of a low-pressure axial flow fan. Due to the limitations of the classical fan design theory on considering the complex 3D internal flow, the spanwise distribution of blade stacking line and section profiles are usually hard to reach the best state. This paper builds a surrogate-assistant multi-objective optimization flow combined with CFD method to explore the optimum blade shape under two typical working conditions. A total of 16 parameters were selected for demonstrating the blade stacking line and section profiles, according to Morris one-at-a-time sensitivity analysis. The objective and constraint functions were the fan's total-to-static efficiency and static pressure rise, respectively. During the optimization, the surrogate models of all response functions were built using kriging models, on which the multi-objective genetic algorithm takes the exploration. The optimization results indicate that the maximum improvement of the efficiency is 1.26 % for low mass flow working condition and 5.47 % for high mass flow working condition. The optimized models tend to make the low-pressure zone distributed along the blade leading edge in the meridian view and to reduce the tip leakage vortex intensity. This paper provides a good practical demonstration of multi-objective fine optimization on the blade shape of a low-pressure axial flow fan.

1. Introduction

The axial-flow fan is one of the most essential and common pieces of equipment in industrial production and daily life. With the international carbon emission reduction plan advancing and the green production requirement increasing, more and more attention has been paid to the aerodynamic performance of low-pressure axial fans. How to finely design and improve fan efficiency has become a widespread concern within the community.

The classical analytical design methods, such as the blade element method (BEM) theory and inverse design method, have limitations on considering the three-dimensional complex flow phenomena inside the fan passage, such as secondary flow, endwall vortex, and tip vortex. Meanwhile, the "trial and error" [1] method also has limited ability to simultaneously deal with dozens of design parameters under multiple working conditions. Stefano [2] historically reviewed the development of aerodynamic design methods for low-speed axial-flow fans and pointed out that the CFD-based numerical optimization approach has become a more advanced fan design method. Many scholars [3-8] have researched applying numerical optimization technology combined with CFD in the turbomachinery optimization process. Due to the large amount of calculation of CFD simulation, the total amount of calculation is often unbearable when the optimization algorithm is directly applied on the simulation method. Thus, a surrogate model is introduced to reduce the CFD calculation times and speed up the optimization. For the axial flow fan field, Lin [9] proposed an integrated method comprising complex optimization method, CFD, and artificial neural network (ANN) to optimize the blade sectional profiles of

an axial-flow fan. Seo [10] optimized the sweep and lean angle of an axial fan blade using a CFD-trained response surface method. Bamberger [11] developed a rapid optimization method for the axial fans based on the evolutionary algorithm, in which the objective function is evaluated by a CFD-trained multilayer perceptron type ANN. These strategies have significantly reduced the optimization cost and acquired effective results, proving the effectiveness of the surrogate-assistant optimization method.

As the core component of a low-pressure axial flow fan, blade shape has a decisive influence on fan performance. The existing researches [12-16] show that changing the blade section profiles and stacking line benefits controlling the blade load distribution, reducing tip vortex flow and secondary flow intensity, and expanding the fan operation range. However, multiple degrees of freedom for the blade shape and complex interaction effects between different shape features make it difficult to further optimize the performance. Some researchers [12, 17] have utilized the optimization design method to improve specific shape features of the axial fan blade, such as blade section profile [18] and stacking line [19-21]. Due to the amount of calculation increasing exponentially as the number of design variables increases, it is still a challenge to finely optimize the multiple blade shape features under multiple operating conditions.

To further improve the low-pressure axial fan's aerodynamic performance under two typical working conditions, this paper carries out a fine optimization on the blade stacking line and section profiles with constraining the pressure rise. Before the optimization, we validated the mesh and simulation settings of the CFD method. A sensitivity analysis using Morris one-at-a-time method was also carried out to filter important parameters from the initial design space. Then, an optimization flow including blade shape parameterization, DOE, CFD simulation, and surrogate-assistant optimizer was established, and a multi-objective optimization design was carried out on the blade stacking line and five section profiles. After the optimization, the Pareto front was acquired, in which three typical Pareto optimum samples were selected. The blade shape, performance and parameters' state of the optimized models were compared and the characteristics of the internal flow were also analyzed.

2. Methodology

2.1 Object of study

The optimization object of this paper is a low solidity low-pressure axial-flow fan USI7. The fan is a rotor-only fan rotating at 3000 rpm with five blades. The USI7 is well designed based on the blade element theory [22] and the section profiles of the blade are 4-digit NACA airfoils, with chord length and relative thickness varying along the spanwise direction. The primary design parameters are presented in Table 1. In 2015, Carolus [23] opened the geometry model (Fig. 1) and detailed performance test data to the fan community.

Table 1. Basic information of the USI7.

Parameters	Value
Design volume flow q_v	0.65 m^3/s
Rotation speed n	3000 rev/min
Number of blades z	5
Shroud diameter D_s	300 mm
Hub to shroud ratio ν	0.45
Tip clearance ratio s / D_s	1.0 %
Chord length of airfoil sections c	68~86 mm
Relative thickness of airfoil sections t	7~8 %
Max. camber of airfoil sections m	4 % (at 0.5 *c*)

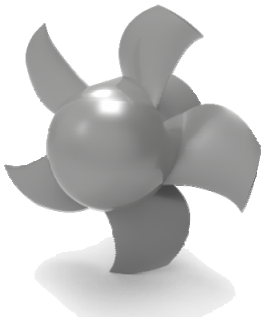

Fig. 1. Geometric rendering of the USI7 rotor.

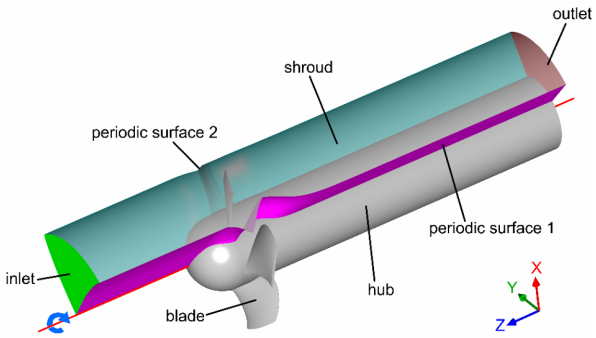

Fig. 2. Schematic diagram of computational domain.

2.2 Numerical simulation method

Before the optimization, the validation of CFD method and settings of the simulation are checked. According to the fan test rig [23] and previous research [24], the inlet and the outlet of the computational domain are set at the $1D_s$ upstream and $2D_s$ downstream the impeller, respectively. A single blade passage is modeled to decrease calculating cost considering the axial symmetry of the fan structure, as shown in Fig. 2. The steady Reynolds-averaged Navier-Stokes (RANS) equations implemented by Fine™/Turbo are applied to solve the flow flied, with low Reynolds number *k-ω* SST turbulence model. A mass flow rate condition is imposed at the inlet and an atmospheric static pressure condition is imposed at the outlet. The convergence criterion level is set to -5.

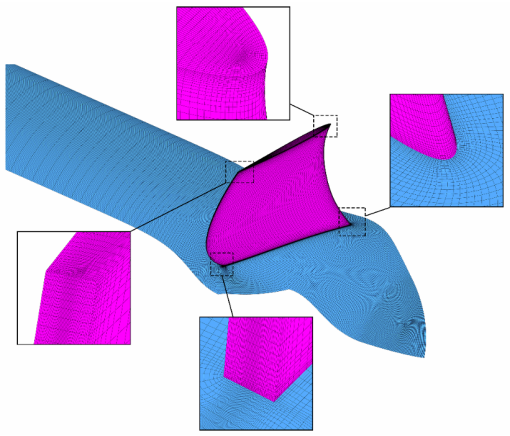

Fig. 3. Mesh details near the blade and hub surfaces.

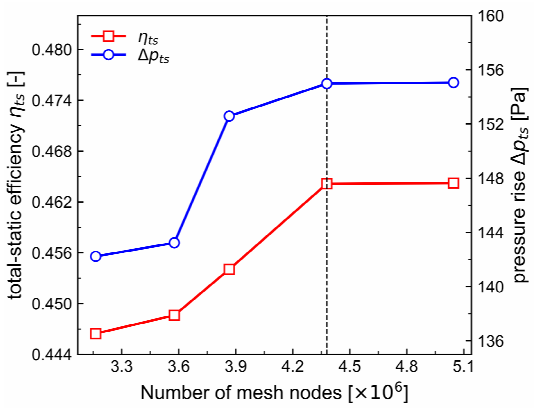

Fig. 4. Mesh independence plot.

A structured mesh grid is generated using Autogrid5, and an O-type topology is applied to the blade surface with non-dimensional wall distance $y^+ < 1$. Fig. 3 shows the mesh details.

Before the formal simulation, a grid independence verification is carried out at five different mesh settings. Fig. 4 presents how the performance metric p_{ts} and η_{ts} (defined in Eqs. (1) and (2)) vary with the mesh size. Considering the validity and calculation cost, the nodes size is finally adopted as 4379066.

With above simulation settings, the CFD predicted aerodynamic performance of the fan was compared with the experimental test data [23] in Fig. 5. The definitions of the total-to-static efficiency η_{ts}, total-to-static pressure rise Δp_{ts} and dimensionless flow coefficient φ are listed in Eqs. (1)-(3). There is an obvious hump on the performance curve of the fan, which is quite common for the rotor-only axial-flow fans. The fan's peak efficiency is near φ = 0.170, and the peak static pressure rise is near φ = 0.153. When the flow coefficient comes below 0.170, the internal flow becomes unstable, making the steady simulation method hard to accurately predict the fan's performance [25]. So only the results of CFD at $\varphi > 0.170$ are kept in this paper, which has max error of 0.025 for the efficiency and 5 Pa for the pressure. The CFD steady

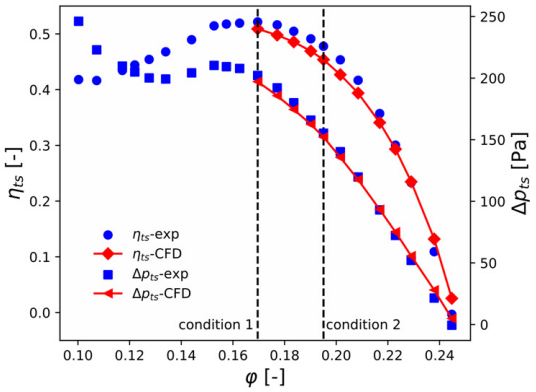

Fig. 5. Simulation and experiment results.

simulation method can be used as the basis of optimization design in this paper.

$$\Delta p_{\mathrm{ts}} = p_{2\mathrm{s}} - p_{1\mathrm{t}} \tag{1}$$

$$\eta_{\mathrm{ts}} = \frac{q_{\mathrm{v}} \Delta p_{\mathrm{ts}}}{P} \tag{2}$$

$$\varphi = \frac{4 q_{\mathrm{v}}}{\pi^2 D^3 n} \tag{3}$$

The optimization goal is to increase fan performance under typical working conditions. The total-to-static efficiency at working condition 1 (φ = 0.170) and condition 2 (φ = 0.195) are selected as the optimization objective functions, marked as η_1 and η_2, respectively. To maintain the pressure performance of the fan, the total-to-statice pressure rises at condition 1 and 2 are used as the optimization constraint functions, marked as p_1 and p_2, respectively. The optimization problem is defined as Eq. (4), where the $\boldsymbol{x}$ is the design parameters vector, and $\boldsymbol{x}_U$ and $\boldsymbol{x}_L$ represents the upper bounds and lower bounds of the design parameters.

$$\begin{aligned} \max \quad & f(\boldsymbol{x}) = \left[\eta_1(\boldsymbol{x}), \eta_2(\boldsymbol{x})\right]^T \\ \text{s.t.} \quad & \boldsymbol{x}_U \geq \boldsymbol{x} \geq \boldsymbol{x}_L \\ & p_1(\boldsymbol{x}) \geq 197.14 \\ & p_2(\boldsymbol{x}) \geq 155.3. \end{aligned} \tag{4}$$

2.3 Blade shape parameterization

A single 3D fan blade is lofted through multiple 2D blade section profiles along the stacking curve, as shown in Fig. 6. In this paper, the stacking point of the profile is at the chord line midpoint. To finely control the blade shape variation, five blade sectional profiles are extracted from 0.0, 0.25, 0.50, 0.75 and 1.0 spans to parameterize the blade shape. The blade geometry is simplified into a fishbone structure. By changing the stacking line, camber curve and side curve of the section profiles, we could finely control the complex variation of the blade shape.

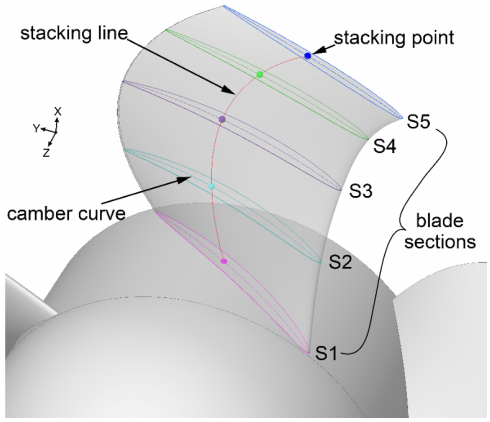

Fig. 6. Diagram of blade geometry forming.

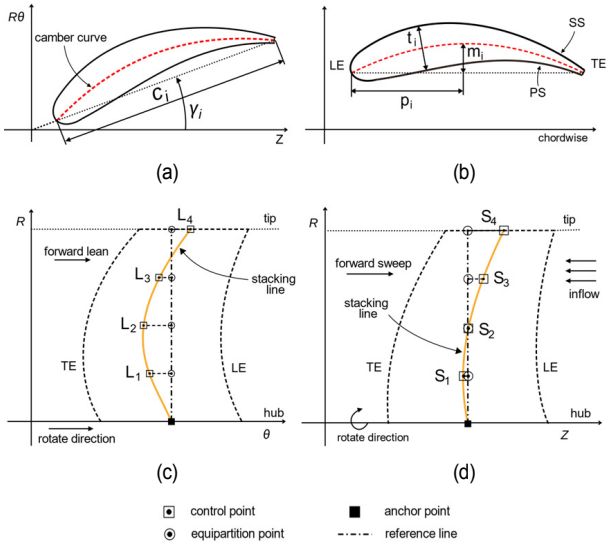

Fig. 7. Schematic diagram of blade shape parameterization.

Fig. 7 presents the parametrization schematic of the blade airfoils and the stacking line. The blade section profile is defined using the NACA 4-digit symmetrical airfoil [26] method, of which the main design parameters are the chord length c_i, the maximum camber m_i, the location of maximum camber p_i, and the maximum thickness t_i. The γ_i is used to define the stagger angle of the airfoil. The subscript $i \in \{1, 2, 3, 4, 5\}$ in these five parameters means the blade section index. Hence, there are 25 parameters to control the variation of the blade section profiles. The 3D stacking line is projected to the meridional plane ($Z-R$) and axial plane ($\theta-R$) for the parameterization convenience, as shown in Figs. 7(c) and (d). The circumferential movement of the blade profile is defined as tangential lean, and the axial movement of the blade profile is defined as axial sweep [27, 28] in this paper. The five points cubic B-spline is used to fit the stacking line. The control points are equidistant distributed along the spanwise direction, and the distance between the control point and the reference radial line starting from the fixed anchor point at the hub, is defined

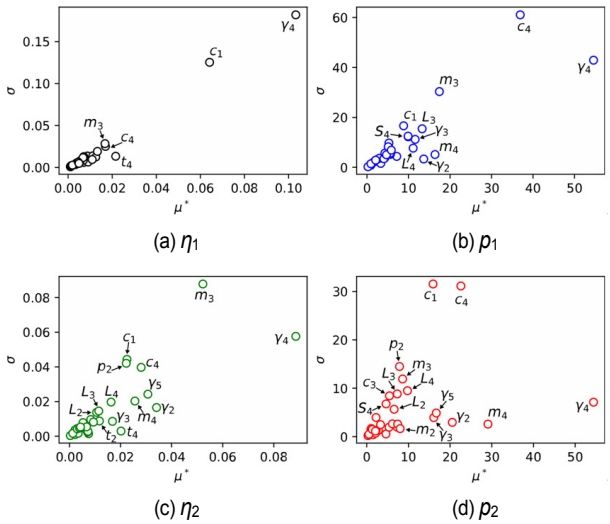

Fig. 8. Standard deviation of elementary effects plotted against modified mean for 33 design parameters.

as the design parameter. The parameter list $[L_1, L_2, L_3, L_4]$ is used to control the lean feature of the stacking line and the list $[S_1, S_2, S_3, S_4]$ is used to control the sweep feature of the stacking line.

Thus, there is a total of 33 parameters to depict the blade shape feature, and it is very difficult and computationally intensive to optimize these parameters at the same time. To remove some parameters with weak influence on the responses, a global sensitivity analysis named Morris one-at-a-time (MOAT) [29] screening method was carried out in this paper. With MOAT, the modified mean μ_i^* indicates the overall effect of a parameter on the response, and the standard deviation σ_i indicates the nonlinear or interaction effects of the parameters. The definitions of the d_i, μ_i^* and σ_i are listed in Eqs. (5), (7) and (8), where $\boldsymbol{x} \in \mathbb{R}^k$ is the design parameters vector and $\boldsymbol{e}_i$ is the i^{th} coordinate vector. In this paper, the number of MOAT levels l is set to 4 and total number of generated samples n is 136.

$$d_i(\boldsymbol{x}) = \frac{y(\boldsymbol{x} + \Delta \boldsymbol{e}_i) - y(\boldsymbol{x})}{\Delta} \tag{5}$$

$$\Delta = \frac{l}{2(l-1)} \tag{6}$$

$$\mu_i^* = \frac{1}{n}\sum_j^n \left| d_i^{(j)} \right| \tag{7}$$

$$\sigma_i = \sqrt{\frac{1}{n}\sum_j^n \left(d_i^{(j)} - \mu_i \right)^2} \tag{8}$$

The distribution of the elementary effects in regard to four response functions is plotted in Fig. 8. Note that a parameter may have different impacts on different response function. For instance, γ_4 has strong nonlinear or interaction effects on η_1, p_1 and η_2, while it has strong linear effects on p_2. Considering the sensitivity of the parameters and the degrees of free-

Table 2. Design parameters with initial values and limits.

x	Lower bound x_L	Baseline	Upper bound x_U
c_1	84	85.5	87
c_4	73	83.0	90
γ_2	58	60.37	64
γ_3	63	64.81	68
γ_4	65	67.30	71
γ_5	65	68.35	72
t_2	0.06	0.0791	0.14
t_4	0.06	0.0734	0.12
m_2	0.023	0.043	0.063
m_3	0.024	0.043	0.064
m_4	0.028	0.05	0.072
p_2	0.3	0.5	0.7
S_4	0.047	0.078	0.107
L_2	0.044	0.0748	0.104
L_3	-0.021	0.0108	0.041
L_4	-0.150	-0.1184	-0.080

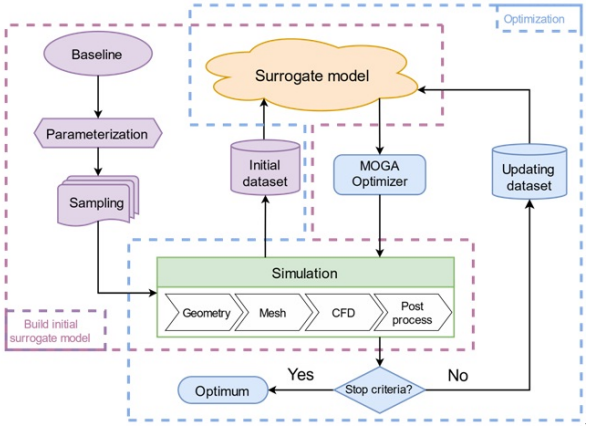

Fig. 9. Optimization flow chart.

dom for blade geometric shape, 16 parameters are filtered from the parameters list. To obtain a reasonable parameter design space, the upper and lower bounds of the design parameters are extended based on the initial parameter values. A small exploration was carried out to confirm the design parameters' limits by the following rules: 1) the geometry modeler could construct proper blade shape; 2) the blade mesh should fulfill the grid quality requirement. The status of final parameter limits is listed in Table 2.

2.4 Optimization flow

To solve the optimization problem, a surrogate-assistant multi-objective optimization flow is built based on the DAKOTA [30] software package. As shown in Fig. 9, the optimization flow includes two steps: build initial surrogate model and optimization explore.

Table 3. Accuracy comparation of different surrogate models based on RMS and cross-validation RMS.

Surrogate model		Kriging	RBF	Polynomial
η_2	RMS	4.42E-17	3.81E-03	6.56E-03
	RMS (LOO)	4.53E-03	7.66E-02	7.62E-03
η_1	RMS	2.45E-17	4.48E-03	1.05E-02
	RMS (LOO)	1.17E-02	9.76E-02	1.21E-02
p_2	RMS	2.88E-14	2.93E+00	2.50E+00
	RMS (LOO)	1.58E-01	5.46E+01	2.93E+00
p_1	RMS	2.01E-14	3.09E+00	8.52E+00
	RMS (LOO)	9.28E-02	8.17E+01	9.83E+00

To build the initial surrogate model, the baseline is parameterized to get the design parameters. Then total 128 samples are drawn from the design space by the Latin hypercube sampling method (LHS). After evaluating the responses of all the sample points, the initial dataset is acquired to train the surrogate model. There are many popular non-linear fitting methods, such as polynomial regression, radial basis function (RBF) networks, kriging model, support vector regression model, and ANN. Some researches [31-33] have evaluated and compared different models' effectiveness and performance. To select a suitable model for the specific problem, we compared the accuracy of three classical surrogates, the kriging [34], RBF, and polynomial regression model, as listed in Table 3. The root mean square (RMS) defined in Eq. (9) was used to evaluate the accuracy. For the surrogate model, we usually pay more attention to the prediction ability of the model. Thus, the leave-one-out (LOO) [35] cross-validation method was applied to calculate the RMS too. Compared to the RBF and polynomial model, the kriging has lower fitting error and higher predicting performance in this paper. Thus, the kriging model was selected to build the surrogate model, and separate models were built for each objective and constraint functions to simplify the surrogate model structure.

$$RMS = \sqrt{\frac{1}{n}\sum_{i=1}^{n}\left(f(x_i)-\hat{f}(x_i)\right)^2} \tag{9}$$

After the initial surrogate model is built, the strength pareto evolutionary algorithm 2 (SPEA2) [36] is used to take the optimization explore on the surrogate. The SPEA2 is a Pareto-based multi-objective evolutionary algorithm (MOEA), whose evolutionary population size, external non-dominated set size, and the mating pool size are set to 400, 50, and 100, respectively. In the selection operation, Deb's constraint tournament selection method [37] is used to handle the constraint of the optimization problem. Although Deb's method does not specify the penalty parameters, it has a strong preference for feasible solutions in the process of individual selection. Thus, it imposes punishment on infeasible solutions to some extent and provides a search direction to the feasible region. The mutation probability is set to 0.01 to maintain the genetic diversity. When

the generation of the population comes to 100, the optimization exploration on the surrogate model is stopped and the final population returns. To maintain the individual diversity of the Pareto set, five individuals are selected from the final population. Then the accurate responses of the two candidates are verified by CFD. The whole optimization loop stops when it comes to the maximum number of design iterations. Otherwise, the five candidates are merged into the updated dataset, used to refresh the surrogate model. The MOEA optimizer continues to explore the updated surrogate model until the stop criterion is satisfied.

The whole optimization calculation is executed on a high-performance computing platform. Two nodes with AMD EPYC 7452 CPU (32-Core@2.3Hz) are utilized to perform the CFD calculation, and total elapsed optimization time is about 190 hours. The maximum number of iterations is 24 and total 120 sample points are evaluated by the CFD simulation.

3. Results

The Pareto front of the optimization is presented in Fig. 10, in which the baseline performance is also marked to show the improvement. Three sample points on the endpoint and midpoint of the pareto optimum are selected to analyze the specific optimization effects. The maximum improvement for η_1 is 1.26 % at model C. The maximum improvement for η_2 is 5.47 % at model A. Model B has moderate improvement for both η_1 and η_2. The specific values of the efficiency are listed in Table 4, in which the pressure rise of conditions 1 and 2 is also compared. The reason why relatively small efficiency improvements bringing higher total-to-static pressure rises will be discussed later. Fig. 11 has a comparison of the performance of the baseline and the optimized models under the stable working conditions. With the flow coefficient increasing, the optimized fans have higher performance improvement.

The final state of the 16 design parameters is presented in Fig. 12. Most of the optimized models' parameters are randomly distributed at both sides of the baseline. While only $L_4, m_3, t_4, t_2, \gamma_5$ and γ_2 concentrate on the one side of the baseline, meaning that the blade shape with better performance tends to have extreme values of the parameter bounds. Thus, the limits of design parameters could be extended in further optimization. Fig. 13 exhibits the blade shape change of the optimized fans. Compared with the baseline, the optimized blades' surfaces are more rugged, owing to the blade section profiles transformation along the streamwise and spanwise directions. For models A and C, the leading edge at blade tip region has changed from pure forward sweep to forward-backward sweep, coming from the stacking line variation. For models B and C, the lean feature shows more complex distri-

Table 4. Performance improvement for the optimized model.

Performance		η_2 [-]	η_1 [-]	p_2 [Pa]	p_1 [Pa]
Baseline		0.464	0.509	155.3	197.14
A	Value	0.489	0.510	192.88	218.25
	Improve	5.47 %	0.20 %	24.20 %	10.71 %
B	Value	0.479	0.512	179.61	205.15
	Improve	3.44 %	0.55 %	15.66 %	4.06 %
C	Value	0.471	0.515	159.01	206.34
	Improve	1.58 %	1.26 %	2.39 %	4.67 %

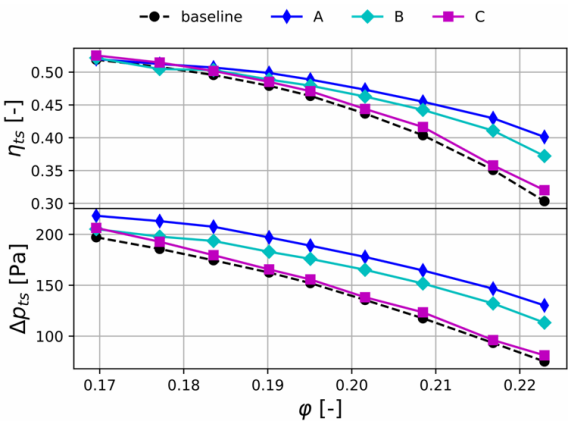

Fig. 11. Aerodynamic performance comparison at $\varphi \in [0.170, 0.223]$.

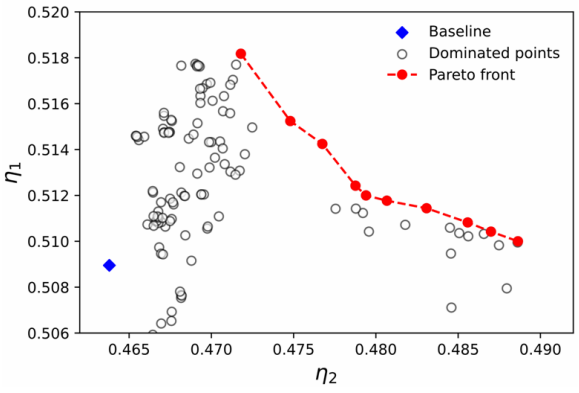

Fig. 10. Pareto front of the optimization problem.

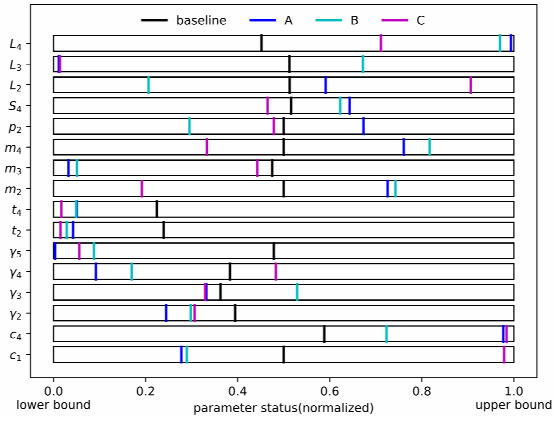

Fig. 12. Parameter state of the optimized blades.

bution. All these characteristics enable the blade to better control the internal flow and improve the aerodynamic performance of the fan.

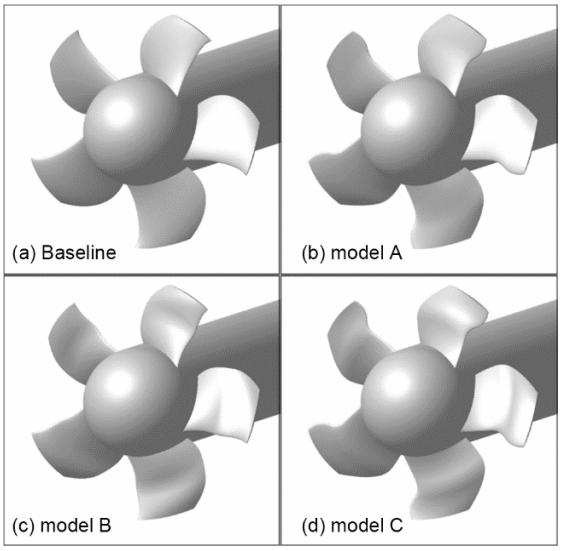

Fig. 13. Blade geometry shape comparison between the baseline and the optimized models.

4. Discussion

To explore the reasons for the fan performance improvement and understand the blade shape change effects on the internal flow, we analyzed the flow field state under the two typical working conditions. Fig. 15 presents the meridional averaged static pressure plot of the optimized fans. Under condition 1, model C (Fig. 14(d)) shows a similar static pressure distribution pattern with the baseline (Fig. 14(a)), and the low-pressure zone at the leading edge and the blade tip is larger than the baseline. The low-pressure zone of models A and B (Figs. 14(b) and (c)) is focused on the top leading edge. By comparing the improvement of η_1 in Table 4, models A and B have the least of the efficiency increase, meaning that the focusing distribution of the low-pressure zone is not a benefit to the efficient transformation of energy. Under condition 2, models A and B's (Figs. 14(f) and (g)) low-pressure zones are distributed along the leading edge, which is similar to the baseline (Fig. 14(a)) and model C (Fig. 14(d)) under condition 1. Meanwhile models A and B (Figs. 14(f) and (g)) have the most of the η_2 improvement. Thus, a simple conclusion can be drawn from this phenomenon: making the low-pressure zone distracting along the blade leading edge by changing the blade shape could improve the energy transformation efficiency of the axial fan.

Fig. 15 shows the blade tip leakage vortex (TLV) and wake

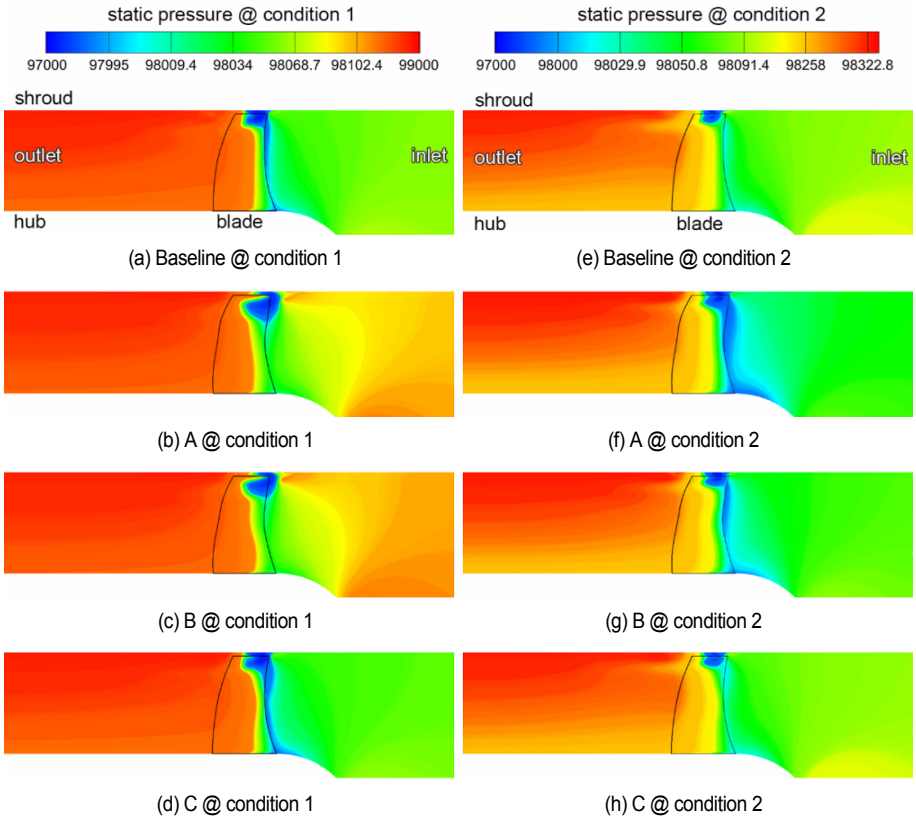

Fig. 14. Meridional averaged static pressure plot.

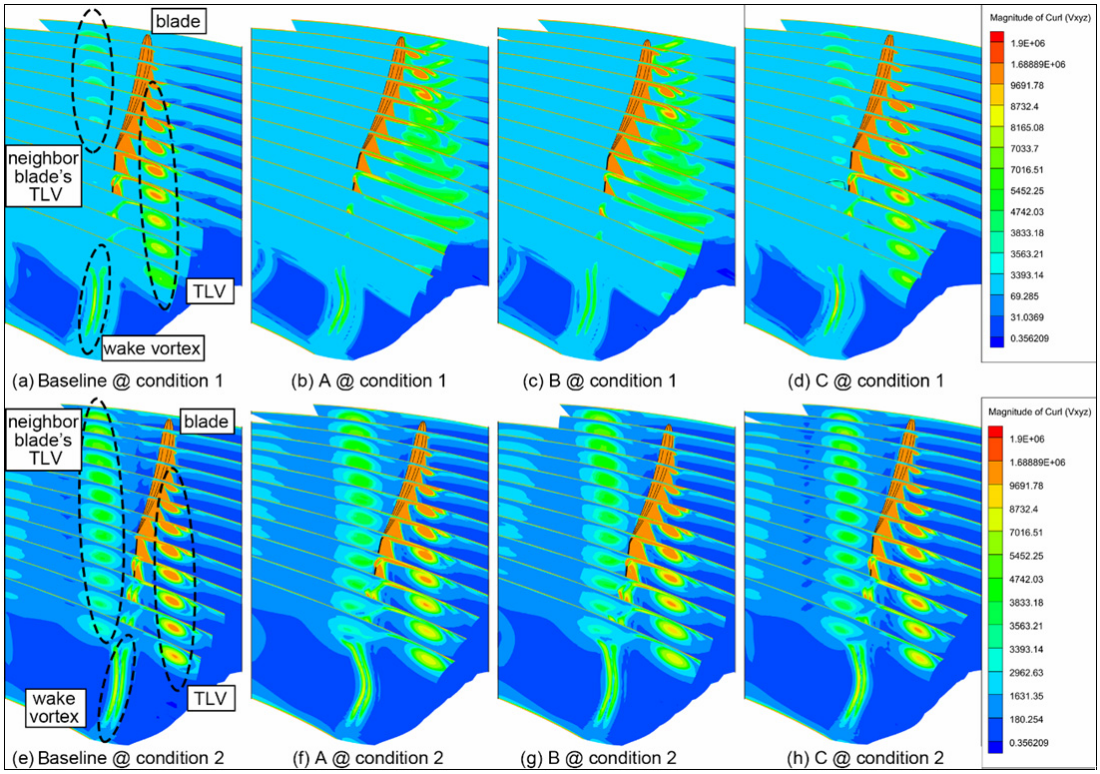

Fig. 15. Velocity curl magnitude plot of blade tip leakage vortex.

vortex variation among baseline and three optimized models. In Fig. 15, the magnitude of velocity curl plotted on the cut planes perpendicular to the blade chord line, is applied to demonstrate the vortex intensity. Under condition 1 (Figs. 15(a)-(d)), the concentration of the A and B models' TLV decreased compared to the baseline and model C. TLV rapidly developed and dissipated within the blade passage, which may block the channel flow and lower the flow efficiency. This could explain why the static pressure obviously increases while the efficiency has almost no improvement for models A and B. Under condition 2 (Figs. 15(e)-(h)), the interacting and mixing position between the neighbor TLV and the wake vortex of the optimized blades are closer to the blade trailing edge, compared to the baseline. This variation comes from the stagger angle change at the tip span, which leads to the wake vortex bending to the blade pressure side. Meanwhile, the TLV intensity of the optimized model A and B is significantly weakened than the baseline, benefiting the flow loss reduction and pressure rise.

The optimized fan models' blade loading distributions at five span locations are plotted in Fig. 16. The blade chord is normalized to [0, 1], meaning that the blade loading starts from the leading edge to the trailing edge. Under condition 1 (Figs. 16(a)-(e)), the obvious variations occur at the blade LE and 0.95 span locations: at the LE region, the pressure side loads of models A and B are decreased, while the static pressure of model A is consistent with the baseline; at the 0.95 span, the optimized blades' loadings at the middle chord and TE locations are both decreased, compared to the baseline. The variation of the blade loading distribution under condition 2 (Figs. 16(f)-(j)) shows a similar pattern to condition 1. The main difference is that the 0.95 span's loads of optimized models A and B are increased near LE, and are decreased near the TE, which will not reduce the total profile loading and helps to main-

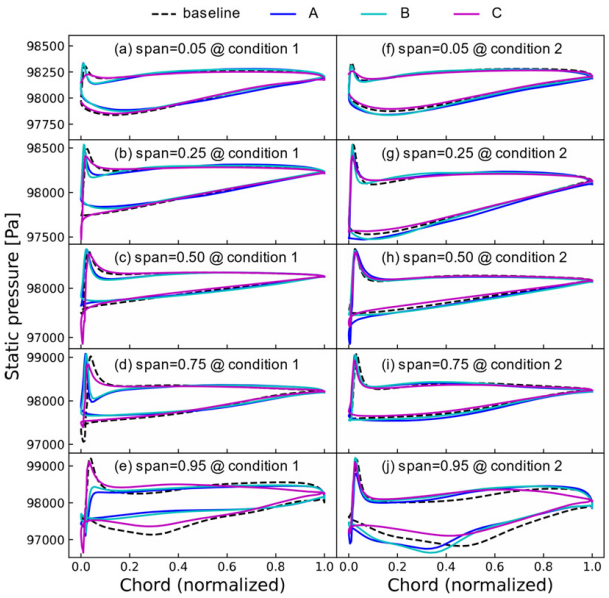

Fig. 16. Blade loading distribution at different span locations (dotted line: baseline, solid line: optimized).

tain the blade's ability to do work. By changing the blade profile shapes, the more reasonable blade loading distribution could be acquired, contributing to loss reduction and efficiency improvement.

The definition of the fan's total-to-static efficiency (Eq. (2)) means that the efficiency is proportional to the static pressure rise ΔP_{ts} and inversely proportional to the shaft power P. Hence, in case of ensuring the constant input shaft power, the increase of static pressure rise of the fan will surely improve the efficiency. However, the true practice of this paper is that the large improvement of the pressure rise dose not bring the equivalent improvement of the efficiency, for example, the p_1 of model A increases by 10.71 % while only 0.21 % increase of η_1 is gained. So, the increase of static pressure rise must have been accompanied by the increase of input power, and the relative relationship between pressure rise and power determines the final efficiency improvement.

5. Conclusion

To further boost the low-pressure axial-flow fan's aerodynamic performance under different working conditions, a surrogate-based multi-objective optimization on the shape of stacking line and blade section profiles was carried out in this paper. After the CFD method validation and the blade shape parameterization, the sensitivity analysis of parameters was carried out using the MOAT method, and total 16 parameters were prepared for the optimization. A surrogate-assistant optimization flow was built, through which the Pareto front of the optimization was acquired.

In the Pareto front, the maximum improvement of the efficiency is 1.26 % for low mass flow working condition and 5.47 % for high mass flow working condition. The efficiency and pressure rise under steady operating conditions also have notable improvements, and with the flow coefficient increasing, the optimized fans have higher performance improvement. By comparing and analyzing three selected pareto optimums, it was found that the optimized blades become more rugged and tend to make the low-pressure zone distributed along the blade leading edge in the meridian view. The changes of the blade stacking line and section profiles improved the blade loading at the leading edge and blade tip sections and reduced the intensity blade tip leakage vortex. These phenomena indicate that the optimized blades have better ability to control the internal flow, which proves that the surrogate-based optimization could effectively improve the aerodynamic performance of the low-pressure axial fans. Thus, this paper may provide a good practical demonstration for multi-objective fine optimization on the blade shape of axial flow fans and help to increase the energy utilization efficiency and promote green production.

Acknowledgments

The authors are grateful to Professor Thomas Carolus for providing the geometry model and experimental test data for USI7.

Nomenclature

CFD	: Computational fluid dynamics
DOE	: Design of experiment
LE	: Leading edge
LOO	: Leave-one-out
MOGA	: Multi-objective genetic algorithm
PS	: Pressure side
RBF	: Radial basis functions
RMS	: Root mean square
SS	: Suction side
TE	: Trailing edge
TLV	: Tip leakage vortex
c_i	: Chord length of blade section profile
D	: Blade tip diameter
p_t	: Total pressure
p_{1t}	: Total pressure at the inlet
p_{2s}	: Static pressure at the outlet
q_v	: Volume flow rate
P	: Shaft power
R	: The R-axis of cylindrical coordinates
$\boldsymbol{x}$	: Design parameter vector
z	: Number of Blades
Z	: The z-axis of cylindrical coordinates
φ	: Flow coefficient
γ_i	: Stagger angle of blade section profile
η_{ts}	: Total-to-static efficiency
θ	: The θ-axis of cylindrical coordinates
Δp_{ts}	: Total-to-static pressure rise

References

[1] K. Bamberger and T. Carolus, Design guidelines for low pressure axial fans based on CFD-trained meta-models, *11th European Conference Turbomachinery Fluid Dynamics and Thermodynamics*, Spain (2015) 1-12.

[2] S. Castegnaro, Aerodynamic design of low-speed axial-flow fans: a historical overview, *Designs*, 2 (3) (2018) 20.

[3] S. Zhou et al., Optimal design of multi-blade centrifugal fan based on partial coherence analysis, *Proceedings of the Institution of Mechanical Engineers, Part C: J. of Mechanical Engineering Science*, 236 (2) (2022) 894-907.

[4] X. Li, Z. Liu and Y. Zhao, Redesign of casing treatment for a transonic centrifugal compressor based on a hybrid global optimization method, *Proceedings of the Institution of Mechanical Engineers, Part C: J. of Mechanical Engineering Science*, 236 (7) (2022) 3398-3417.

[5] D. Sakaguchi et al., Global optimization of recirculation flow type casing treatment in centrifugal compressors of turbochargers, *Proceedings of the Institution of Mechanical Engineers, Part C: J. of Mechanical Engineering Science*, 232 (24) (2018) 4461-4471.

[6] J.-H. Kim, J.-H. Choi and K.-Y. Kim, Surrogate modeling for

optimization of a centrifugal compressor impeller, *International J. of Fluid Machinery and Systems*, 3 (1) (2010) 29-38.

[7] S. Kim et al., Design optimization for mixed-flow pump impeller by improved suction performance and efficiency with variables of specific speeds, *Journal of Mechanical Science and Technology*, 34 (6) (2020) 2377-2389.

[8] S. Kim et al., Design optimization of mixed-flow pump impellers with various shaft diameters at the same specific speed, *Journal of Mechanical Science and Technology*, 32 (3) (2018) 1171-1180.

[9] B.-J. Lin, C.-I. Hung and E. J. Tang, An optimal design of axial-flow fan blades by the machining method and an artificial neural network, *Proceedings of the Institution of Mechanical Engineers, Part C: J. of Mechanical Engineering Science*, 216 (3) (2002) 367-376.

[10] S. J. Seo, S. M. Choi and K. Y. Kim, Design optimization of a low-speed fan blade with sweep and lean, *Proceedings of the Institution of Mechanical Engineers, Part A: J. of Power and Energy*, 222 (1) (2008) 87-92.

[11] K. Bamberger and T. Carolus, Development, application, and validation of a quick optimization method for the class of axial fans, *J. of Turbomachinery*, 139 (11) (2017) 111001.

[12] P. Song and J. Sun, Blade shape optimization for transonic axial flow fan, *Journal of Mechanical Science and Technology*, 29 (3) (2015) 931-938.

[13] J. Vad, G. Halász and T. Benedek, Efficiency gain of low-speed axial flow rotors due to forward sweep, *Proceedings of the Institution of Mechanical Engineers, Part A: J. of Power and Energy*, 229 (1) (2015) 16-23.

[14] A. Nazmi Ilikan and E. Ayder, Influence of the sweep stacking on the performance of an axial fan, *J. Turbomach*, 137 (6) (2015) 61004.

[15] F. Zenger, A. Lorenz and S. Becker, Experimental investigation of the flow-and sound-field of low-pressure axial fans with different blade stacking strategies, *17th International Symposium on Transport Phenomena and Dynamics of Rotating Machinery (ISROMAC2017)*, Maui, United States (2017).

[16] L. Zhang, Y.-Z. Jin and Y.-Z. Jin, An investigation on the effects of irregular airfoils on the aerodynamic performance of small axial flow fans, *J. Mech. Sci. Technol*, 27 (6) (2013) 1677-1685.

[17] R. A. Adjei et al., Multidisciplinary design optimization for performance improvement of an axial flow fan using free-form deformation, *J. of Turbomachinery*, 143 (1) (2020).

[18] P. Song, J. Sun and K. Wang, Blade shape optimization of transonic axial flow fan in terms of sectional profiles and stacking line, *Turbo Expo: Power for Lank, Sea, and Air,* Düsseldorf, Germany (2014).

[19] W. Yue, Y. Jin and Z. Wen, Multiobjective optimization design for skew and sweep parameters of two-stage blades of axial fan, *ISRN Mechanical Engineering*, 2013 (2013).

[20] C. Kong et al., An optimization on the stacking line of low-pressure axial-flow fan using the surrogate-assistant optimization method, *J. Mech. Sci. Technol*, 35 (11) (2021) 4997-5005.

[21] T. Ding et al., Optimization design of agricultural fans based on skewed-swept blade technology, *Applied Engineering in Agriculture*, 35 (2) (2019) 249-258.

[22] T. H. Carolus and R. Starzmann, An aerodynamic design methodology for low pressure axial fans with integrated airfoil polar prediction, *Proceedings of the ASME Turbo Expo 2011*, Vancouver, Canada (2011).

[23] T. Carolus, T. Zhu and M. Sturm, A low pressure axial fan for benchmarking prediction methods for aerodynamic performance and sound, *Noise Control Engineering J.*, 63 (6) (2015) 537-545.

[24] T. Zhu and T. H. Carolus, Experimental and numerical investigation of the tip clearance noise of an axial fan, *Proceedings of ASME Turbo Expo 2013,* San Antonio, Texas, USA (2013).

[25] T. Zhu and T. H. Carolus, Experimental and unsteady numerical investigation of the tip clearance noise of an axial fan, *ASME 2013 Turbine Blade Tip Symposium,* ASME, Hamburg, Germany (2013) V001T04A001.

[26] E. N. Jacobs, K. E. Ward and R. M. Pinkerton, *The Characteristics of 78 Related Airfoil Sections from Tests in the Variable-Density Wind Tunnel*, Langley Memorial Aeronautical Laboratory (1933).

[27] J. Vad, Forward blade sweep applied to low-speed axial fan rotors of controlled vortex design: an overview, *J. Eng. Gas. Turbines Power-Trans. ASME*, 135 (1) (2013) 012601.

[28] M. Masi and A. Lazzaretto, A simplified theory to justify forward sweep in low hub-to-tip ratio axial fan, *ASME Turbo Expo 2015: Turbine Technical Conference and Exposition*, Montreal, Quebec, Canada (2015).

[29] M. D. Morris, Factorial sampling plans for preliminary computational experiments, *Technometrics*, 33 (2) (1991) 161-174.

[30] B. M. Adams et al., *Dakota, A Multilevel Parallel Object-Oriented Framework for Design Optimization, Parameter Estimation, Uncertainty Quantification, and Sensitivity Analysis: Version 614 User's Manual*, Sandia National Lab. (SNL-NM) (2021).

[31] A. Bhosekar and M. Ierapetritou, Advances in surrogate based modeling, feasibility analysis, and optimization: A review, *Computers and Chemical Engineering*, 108 (2018) 250-267.

[32] S. Bagheri, W. Konen and T. Bäck, Comparing Kriging and radial basis function surrogates, *Proc. 27. Workshop Computational Intelligence* (2017) 243-259.

[33] R. Jin, W. Chen and T. W. Simpson, Comparative studies of metamodelling techniques under multiple modelling criteria, *Struct Multidisc Optim*, 23 (1) (2001) 1-13.

[34] A. Giunta and L. Watson, A comparison of approximation modeling techniques-polynomial versus interpolating models, *7th AIAA/USAF/NASA/ISSMO Symposium on Multidisciplinary Analysis and Optimization* (1998) 4758.

[35] M. Meckesheimer et al., Computationally inexpensive metamodel assessment strategies, *AIAA J.*, 40 (10) (2002) 2053-2060.

[36] E. Zitzler, M. Laumanns and L. Thiele, *SPEA2: Improving the Strength Pareto Evolutionary Algorithm*, Swiss Federal Institute of Technology, Switzerland (2001).

[37] K. Deb, An efficient constraint handling method for genetic algorithms, *Computer Methods in Applied Mechanics and Engineering*, 186 (2-4) (2000) 311-338.

Chuang Kong is currently a Ph.D. candidate in the Institute of Process Equipment, College of Energy Engineering, Zhejiang University, China. He received his B.S. from Dalian University of Technology, China, in 2016. His research interests include computational fluid dynamics and design optimization of turbomachinery.

Tao Jin is currently a Professor at Zhejiang University, China. He received his B.S. from Zhejiang University in 1985, and M.S. and Ph.D. in Chemical Engineering from the same university in 1989 and 2000, respectively. His research interests include fluid machinery, computational aided design, and computational aided engineering.